

SAIP: A PLUG-AND-PLAY SCALE-ADAPTIVE MODULE IN DIFFUSION-BASED INVERSE PROBLEMS

Lingyu Wang, Xiangming Meng*

Zhejiang University, ZJU-UIUC Institute, Haining, China

ABSTRACT

Solving inverse problems with diffusion models has shown promise in tasks such as image restoration. A common approach is to formulate the problem in a Bayesian framework and sample from the posterior by combining the prior score with the likelihood score. Since the likelihood term is often intractable, estimators like DPS, DMPS, and π GDM are widely adopted. However, these methods rely on a fixed, manually tuned scale to balance prior and likelihood contributions. Such a static design is suboptimal, as the ideal balance varies across timesteps and tasks, limiting performance and generalization. To address this issue, we propose SAIP, a plug-and-play module that adaptively refines the scale at each timestep without retraining or altering the diffusion backbone. SAIP integrates seamlessly into existing samplers and consistently improves reconstruction quality across diverse image restoration tasks, including challenging scenarios.

Index Terms— Inverse problems; diffusion models; optimal scale; image restoration

1. INTRODUCTION

Image restoration is a typical inverse problem that aims to recover a clean, high-quality image $x \in \mathbb{R}^{N \times 1}$ from a degraded observation $y \in \mathbb{R}^{M \times 1}$. Depending on the degradation process, typical tasks include denoising [1], deblurring [2], and inpainting [3], all of which can be cast as a linear inverse problem:

$$y = Ax + n, \quad (1)$$

where $A \in \mathbb{R}^{M \times N}$ is a linear forward operator and $n \sim \mathcal{N}(0, \sigma^2 I)$ denotes Gaussian noise. Due to system limitations and environmental disturbances, the measurement y is often incomplete, noisy, or otherwise degraded. The resulting ill-posedness generally implies non-uniqueness of the solution x , making restoration fundamentally challenging. To resolve this ambiguity and select a plausible solution, one must incorporate prior knowledge or regularization about the target signal. From a Bayesian perspective [4], this amounts to performing posterior inference $p(x | y)$ via Bayes' rule,

$$p(x | y) \propto p(x) p(y | x), \quad (2)$$

where $p(x)$ and $p(y | x)$ are the prior and the likelihood, respectively. The prior $p(x)$ encapsulates assumptions about natural images and thus plays a central role in inverse problems. Classical choices include hand-crafted, analytical priors (e.g., sparsity [5],

This work has been submitted to the IEEE for possible publication. Copyright may be transferred without notice, after which this version may no longer be accessible.

*Corresponding author

low-rank structure [6], and total variation [5]) as well as architecture-induced priors such as the Deep Image Prior [7]. However, these priors often fall short of capturing the full complexity of natural images. Recently, generative models, especially diffusion models [8, 9], have emerged as powerful data-driven priors for inverse problems [10, 2, 11, 12, 13, 14, 15, 16]. Following Bayes' rule (2), posterior inference with diffusion models requires the posterior score:

$$\nabla_{x_t} \log p(x_t | y) = \nabla_{x_t} \log p(x_t) + \lambda \nabla_{x_t} \log p(y | x_t), \quad (3)$$

where x_t is a noisy latent in the diffusion process and λ is a scaling factor. The prior score $\nabla_{x_t} \log p(x_t)$ is provided by the pretrained diffusion model, whereas the likelihood score $\nabla_{x_t} \log p(y | x_t)$ is generally intractable [2, 17, 11, 10]. A number of approximations have been proposed, including Diffusion Posterior Sampling (DPS) [10], Pseudoinverse-Guided Diffusion Models (π GDM) [12], and Diffusion Model Posterior Sampling (DMPS) [11].

Despite their success, existing methods typically rely on a fixed, manually tuned λ to balance the prior and likelihood contributions. This practice is tedious and often suboptimal. As observed in DMPS [11], the final reconstruction quality is highly sensitive to λ : even small deviations can markedly degrade sampling performance or lead to instability. Moreover, a single, manually chosen coefficient lacks robustness across noise levels and timesteps, necessitating extensive per-setting tuning. This not only reduces efficiency but also exposes λ selection as a key bottleneck that limits the stability and generalization of current diffusion-based inverse solvers.

To address this, inspired by the self-adaptive guidance in CFG-Zero* [18] for conditional generation, we extend the idea to inverse problems and propose a self-adaptive scaling module (**SAIP**). SAIP dynamically estimates λ during inference, allowing the guidance strength at each timestep to adapt to task and noise specific characteristics, thereby combining prior and likelihood in a more robust manner. SAIP is plug-and-play: it integrates into existing diffusion-based inverse problem solvers without retraining or modifying the diffusion backbone. Comparisons between the baseline and its "SAIP +" version are shown in Fig. 1.

The main contributions are summarized as follows:

(1) We extend the idea of adaptive scaling to inverse problems and introduce SAIP, a plug-and-play module that dynamically estimates the scale during inference. To the best of our knowledge, this is the first work to introduce adaptive scaling into diffusion-based inverse problem solvers. SAIP also can be directly applied to a wide range of methods that combine estimated likelihood and prior scores, such as DiffStateGrad [19], without retraining.

(2) We integrate SAIP into several representative diffusion-based solvers and evaluate it on classical image restoration tasks. Experiments span both standard settings and more challenging scenarios with severe degradation, high noise and latent domain. The results demonstrate consistent improvements over nearly all baselines, while incurring only a minor additional inference cost.

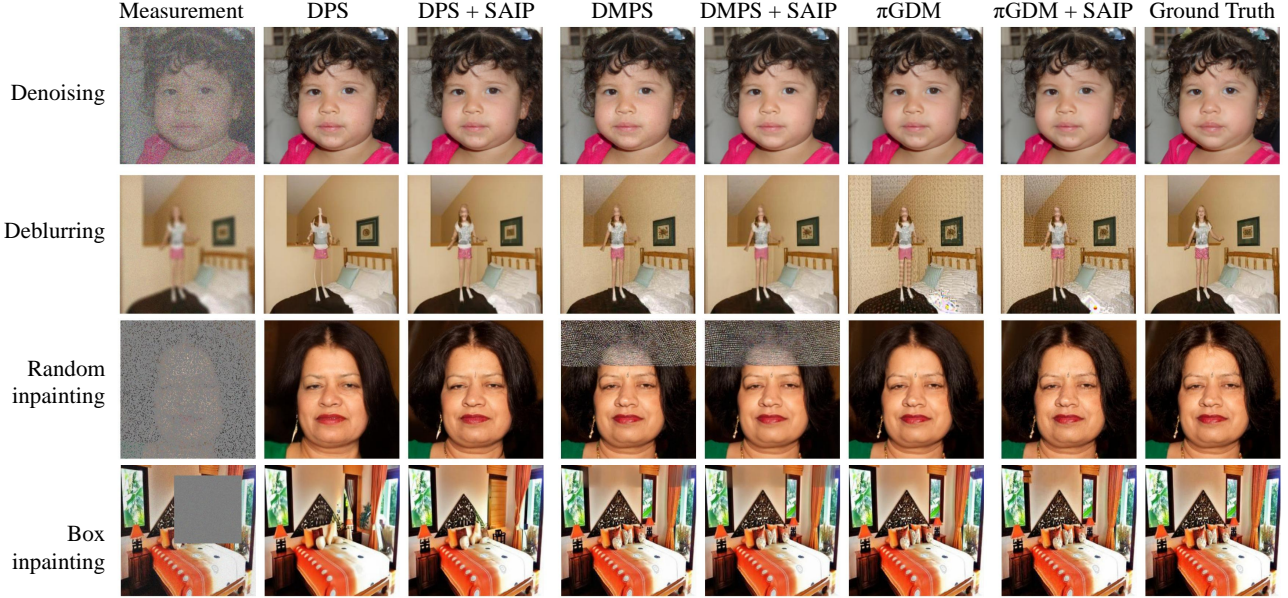


Fig. 1: Representative results. Rows 1 and 3: FFHQ at 256×256 ; Rows 2 and 4: LSUN-Bedroom at 256×256 .

2. METHOD

To address the fixed scale challenge in diffusion-based inverse problem solvers, we propose a plug-and-play module called **SAIP**, which dynamically adjusts the balance between the prior and likelihood scores during posterior sampling.

Our design is inspired by the self-adaptive guidance introduced in CFG-Zero* [18] for classifier-free guidance [20]:

$$\nabla_{x_t} \log \tilde{p}(x_t|y) = \omega \nabla_{x_t} \log p(x_t|y) + s(1 - \omega) \nabla_{x_t} \log p(x_t), \quad (4)$$

where ω is the guidance strength and s is a learnable scaling factor.

To adapt this idea to inverse problems, we replace the posterior score in right side of Eq.(4) with the sum of the likelihood score and the prior score.

$$\nabla_{x_t} \log \tilde{p}(x_t|y) = [s(1 - \omega) + \omega] \nabla_{x_t} \log p(x_t) + \omega \nabla_{x_t} \log p(y|x_t). \quad (5)$$

Then, we reorganize the equation by factoring out the prior score term with a coefficient of 1 from the posterior score expression.

$$\begin{aligned} \nabla_{x_t} \log \tilde{p}(x_t|y) &= \underbrace{\nabla_{x_t} \log p(x_t) + \omega \nabla_{x_t} \log p(y|x_t)}_{\text{as same as Eq. (3) when } \omega = \lambda} \\ &+ \underbrace{[(s - 1)(1 - \omega)] \nabla_{x_t} \log p(x_t)}_{\text{Additional part}}, \end{aligned} \quad (6)$$

Thus, compared to Eq. (3), the SAIP formulation essentially adds an adaptive offset $(s - 1)(1 - \omega)$ to the prior score, making it possible to refine the balance between the two components adaptively. **In particular, when setting $s = 1$, Eq. (6) reduces to the original formulation of the baseline method.**

The remaining problem is to calculate s , we minimize the gap between the estimated posterior score and the ground-truth posterior score:

$$\mathcal{L}(s) = \|\nabla_{x_t} \log \tilde{p}(x_t|y) - \nabla_{x_t} \log p^*(x_t|y)\|^2, \quad (7)$$

where the first term is the estimated posterior score modulated by SAIP, as defined in Eq. (5), and $p^*(x_t|y)$ denotes the true posterior. Since p^* is intractable, We replace the posterior score in Eq. (6) and introduce a new parameter $\omega^* = \omega - 1$, which allows us to rewrite the loss as

$$\mathcal{L}(s) = \left\| \nabla_{x_t} \log \tilde{p}_\theta(x_t|y) - \nabla_{x_t} \log p^*(x_t|y) + \omega^* (-s \nabla_{x_t} \log p(x_t) + \nabla_{x_t} \log p(y|x_t)) \right\|^2. \quad (8)$$

Applying the triangle inequality, we obtain

$$\begin{aligned} \mathcal{L}(s) &\leq \|\nabla_{x_t} \log p_\theta(x_t|y)\|^2 + \|\nabla_{x_t} \log p^*(x_t|y)\|^2 \\ &\quad + \|\omega^* (-s \nabla_{x_t} \log p(x_t) + \nabla_{x_t} \log p(y|x_t))\|^2, \end{aligned} \quad (9)$$

which shows that minimizing $\mathcal{L}(s)$ is equivalent to minimizing the upper-bound

$$\mathcal{L}_{\text{upper}} = \|-s \nabla_{x_t} \log p(x_t) + \nabla_{x_t} \log p(y|x_t)\|^2. \quad (10)$$

To minimize the $\mathcal{L}_{\text{upper}}$, we take the derivative with respect to s and set it to zero:

$$\begin{aligned} \frac{d}{ds} \mathcal{L}_{\text{upper}} &= 2s \|\nabla_{x_t} \log p(x_t)\|^2 \\ &\quad - 2 \langle \nabla_{x_t} \log p(x_t), \nabla_{x_t} \log p(y|x_t) \rangle = 0. \end{aligned} \quad (11)$$

Finally, we obtain the closed-form optimal value of s .

$$s = \frac{\langle \nabla_{x_t} \log p_\theta(x_t|y), \nabla_{x_t} \log p_\theta(x_t) \rangle}{\|\nabla_{x_t} \log p_\theta(x_t)\|^2}, \quad (12)$$

which can be computed in closed form. It is worth noting that **the additional cost of SAIP is very low**, and adding SAIP does not increase the additional reasoning cost. More detailed discussions on time and memory consumption can be found in Section 3.2.3.

3. EXPERIMENTS

In this section, we conduct experiments on several inverse problems to evaluate the effectiveness of the proposed **SAIP** module. The code is available at: <https://github.com/seulaugues/SAIPcode>.

3.1. Experimental Setup

3.1.1. Tasks.

Standard: (a) Uniform deblurring [2] with a 9×9 uniform kernel; (b) Denoising [1] with Gaussian noise ($\sigma = 0.5$); (c) Random inpainting [3] with 90% missing pixels; (d) Box inpainting [3] with a 128×128 square mask. A mild Gaussian noise ($\sigma = 0.05$) is added in all cases except denoising.

Challenging: (a) Intensified degradation: $\sigma = 0.9$ denoising, 191×191 box inpainting, and 99% random inpainting; (b) High-level noise injection: Gaussian noise increased from $\sigma = 0.05$ to 0.5 for deblurring/inpainting. (c) Latent domain and nonlinear transfer: Based on DiffStateGrad [19] + Resample (main sampler) [21], 128×128 box inpainting, 70% random inpainting, and $2 \times$ high dynamic range.

3.1.2. Other Details.

Datasets are FFHQ [22] and LSUN-bedroom [23] (256×256), which we conducted experiments on. We adopt pretrained ADM diffusion models[24] (FFHQ from Google Drive, LSUN-bedroom from OpenAI GitHub). Baselines include DPS, DMPS, and π GDM, with "SAIP +" versions denoted DPS+SAIP, DMPS+SAIP, and π GDM+SAIP. Performance is evaluated using PSNR[25], SSIM [26], and LPIPS [27], and all experiments are run on a single NVIDIA RTX 4090.

3.2. Results

3.2.1. Qualitative results.

Fig. 2 presents representative qualitative results under challenging conditions. For subplot (a), the integration of DPS effectively removes the artifact on the right side and yields a subject appearance more consistent with the ground truth. In the case of π GDM, it successfully eliminates the large green background region, resulting in a more natural subject. For subplot (b), DPS removes the eyeglasses and introduces bangs compared to the baseline, while DMPS produces a smoother transition around the mask box on the subject's head. For subplot (c), incorporating SAIP into DPS leads to sharper details and more pronounced facial wrinkles, DMPS directly removes the box artifact, and π GDM reduces the residual box region in the upper part of the image. For subplot (d), SAIP enhances DPS by generating clearer textures and distinct boundaries on the subject's fingers, while in DMPS, SAIP suppresses sharp artifacts and yields a smoother overall appearance.

Across all examples, SAIP consistently improves reconstruction quality over baselines, producing better structural fidelity, coherent textures, and perceptual realism, even under extreme degradations. Under both standard and high-level noise settings, integrating SAIP consistently improves the best performing baseline methods across denoising, deblurring, and inpainting tasks.

3.2.2. Quantitative results.

Table 4: Quantitative comparison on FFHQ 256×256 validation dataset under intensified degradation tasks (type a).

Task	PSNR \uparrow	LPIPS \downarrow	SSIM \uparrow
Denoise (DMPS) + SAIP	25.32 25.82	0.3208 0.2669	0.6529 0.7185
Random Inpaint (DPS) + SAIP	18.54 20.19	0.4295 0.3467	0.4968 0.5843
Box Inpaint (DMPS) + SAIP	16.37 19.76	0.2669 0.2455	0.7539 0.8133

We present a quantitative comparison based on standard and challenging evaluation settings. Table 1 reports the reconstruction performance of different algorithms on the FFHQ 256×256 dataset under standard settings, while supplementary experiments on the LSUN-bedroom dataset (Table 3) further confirm that SAIP consistently enhances the performance of all baseline methods. Note that for consistency, all reported numbers are mean values, as the variance is slightly lower than that of the baselines. Due to space constraints, only a subset of the LSUN results is reported.

In challenging settings, SAIP consistently improves upon baseline methods, as summarized in Table 4, Table 2, and Table 5. Even under conditions with severe degradations, strong noise interference, or operation in the latent domain, SAIP demonstrates clear gains over the original solvers. These results indicate that SAIP is not confined to particular types of diffusion-based methods, but can be effectively applied across diverse restoration scenarios, spanning both pixel- and latent-domain formulations. The observed improvements further highlight its applicability, adaptability to different tasks, and robustness under both linear and nonlinear degradation conditions.

Table 5: Challenging tasks (type c) on DiffStateGrad + Resample (origin, FFHQ 256×256 dataset).

Task	PSNR \uparrow	LPIPS \downarrow	SSIM \uparrow
Random Inpaint (Origin) + SAIP	31.20 31.36	0.1621 0.1587	0.8925 0.8966
Box Inpaint (Origin) + SAIP	21.07 21.06	0.2501 0.2477	0.7828 0.7839
HDR (Origin) + SAIP	24.60 24.71	0.2840 0.2824	0.7706 0.7736

3.2.3. Computational Overhead.

As shown in Table 6, all experiments are conducted on a single NVIDIA RTX 4090 for denoising on FFHQ, and incorporating SAIP increases per-image inference time by 0.5s and memory usage by 3MB, which is modest and acceptable in practice.

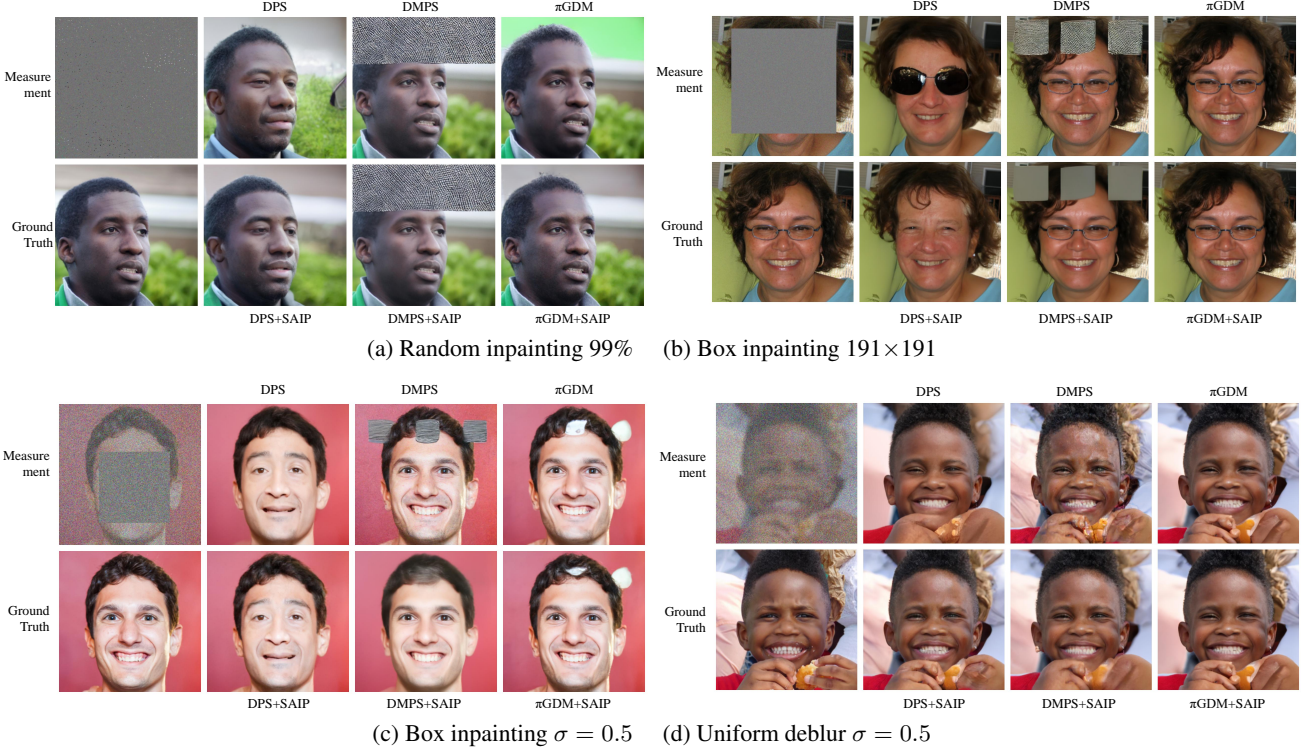


Fig. 2: Challenging results for different inverse tasks.

Table 6: Runtime (s) and memory consumption (MB) for different algorithms on the FFHQ dataset for the denoising task.

Metric	DPS / +SAIP	DMPS / +SAIP	π GDM / +SAIP
Time	90.01 / 90.32	32.67 / 33.00	73.04 / 73.65
Memory	5449 / 5453	4492 / 4496	2782 / 2785

3.3. S-Curve Analysis

Fig. 3 shows the adaptive scale s along the reverse diffusion trajectory ($t = 1000$ to 0) under the same DDPM [28] schedule. Subplots (a) and (b) show successful cases, while (c) shows a failure case. The denoising task is used as a example, since s trends similarly across tasks, and the π GDM curve closely follows DPS and is omitted.

Across all cases, s initially deviates from 1 and gradually returns as the process progresses, reflecting early-stage inaccuracies of the likelihood score estimator [10, 11, 12]. By balancing prior and likelihood, s mitigates the bias and eventually converges toward 1.

The key difference between success and failure lies in early stage and mid stage behavior. In successful cases (Fig. 3a,b), s corrects the likelihood bias immediately and stabilizes, preventing error accumulation and enabling accurate reconstructions. In contrast, the failure case (Fig. 3c) also exhibits an initial oscillation, but its duration is short, after which s remains with only small fluctuations around 1. It only resumes noticeable activity in the middle stage, by which time the trajectory has already deviated from the optimal path. This delayed response limits SAIP’s corrective power and ultimately leads to a failed reconstruction. These results indicate that prompt early adjustment of s is critical for SAIP’s success.

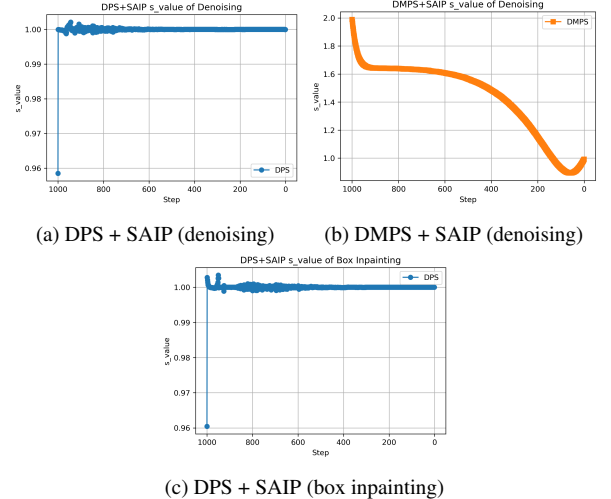


Fig. 3: Scale s for SAIP across different methods and tasks. Figures (a) and (b) present successful cases, (c) shows a failure case.

4. CONCLUSION AND DISCUSSION

SAIP mechanism. The core idea of SAIP is to compute a closed-form adaptive guidance scale s by projecting the mismatch between the posterior score and the prior score onto the prior-score direction. This formulation provides three properties: (a) in the early stages of sampling, when the estimated likelihood score is often noisy, s de-

Table 1: Quantitative comparison on different tasks under standard settings on 1k images of the FFHQ 256×256 dataset. We report only mean values for clarity, as SAIP shows the variance comparable to or slightly smaller than that of the baselines. Best results are in **bold**.

Method	Denoising			Deblurring			Random inpainting			Box inpainting		
	PSNR	LPIPS	SSIM	PSNR	LPIPS	SSIM	PSNR	LPIPS	SSIM	PSNR	LPIPS	SSIM
DPS + SAIP	27.47 27.50	0.2405 0.2365	0.7737 0.7796	25.36 27.18	0.2576 0.2028	0.7184 0.7863	24.32 26.83	0.2915 0.1967	0.7067 0.8090	23.31	0.2148	0.7993
DMPS + SAIP	27.76 28.15	0.2473 0.2098	0.7628 0.8034	27.25 27.47	0.2241 0.2194	0.7681 0.7877	16.47 17.27	0.3356 0.3299	0.6581 0.6720	20.15 24.86	0.1766 0.1737	0.8641 0.8866
π GDM + SAIP	27.28 27.30	0.2311 0.2301	0.7814 0.7817	27.10 27.12	0.2225 0.2226	0.7700 0.7708	30.43 30.97	0.1393 0.1260	0.8919 0.8996	28.51 28.81	0.1044 0.1091	0.9220 0.9210

Table 2: Quantitative comparison on FFHQ 256×256 validation dataset under high-level noise challenging tasks (type b): **Denoising** with $\sigma = 0.9$; **other tasks** with Gaussian noise $\sigma = 0.5$. Best results are in **bold**.

Method	Denoising			Deblurring			Random inpainting			Box inpainting		
	PSNR	LPIPS	SSIM	PSNR	LPIPS	SSIM	PSNR	LPIPS	SSIM	PSNR	LPIPS	SSIM
DPS + SAIP	25.00 25.17	0.3018 0.2913	0.6809 0.6963	22.28 24.55	0.3359 0.2839	0.6089 0.6793	19.41 22.52	0.4194 0.3381	0.5215 0.6167	21.42 21.52	0.3159 0.2849	0.6570 0.6920
DMPS + SAIP	25.32 25.82	0.3208 0.2669	0.6529 0.7185	21.94 23.04	0.3725 0.3175	0.5329 0.6268	16.10 16.88	0.4521 0.3984	0.5149 0.6398	20.11 22.04	0.3341 0.3188	0.6688 0.7002
π GDM + SAIP	24.61 24.72	0.2985 0.2927	0.6827 0.6893	21.29 21.79	0.3592 0.3410	0.5544 0.5803	24.92 24.95	0.2703 0.2692	0.7251 0.7254	25.16	0.2476 0.2469	0.7579 0.7569

Table 3: Part of supplementary results on LSUN-bedroom 256×256 dataset.

Task	PSNR \uparrow	LPIPS \downarrow	SSIM \uparrow
Denoise (DMPS) + SAIP	26.94 27.77	0.3052 0.2234	0.7177 0.8106
Deblur (π GDM) + SAIP	24.83 25.98	0.2854 0.2483	0.6900 0.7541
Random Inpaint (π GDM) + SAIP	29.64 32.64	0.1465 0.0992	0.8974 0.9325
Box Inpaint (π GDM) + SAIP	26.64 28.49	0.1081 0.0909	0.9273 0.9332

viates from 1 to emphasize the contribution of the prior and prevent error accumulation; (b) as alignment improves during sampling, s naturally converges toward 1, effectively recovering the behavior of the baseline method and ensuring stability; (c) in rare cases of score anti-alignment, s may take transient negative values, which act as a corrective mechanism that stabilizes the trajectory.

Conclusion. We propose SAIP, a plug and play module that adaptively scales the balance between prior and (approximated) likelihood in diffusion based inverse problem solvers. In addition to integration with DPS, DMPS, and π GDM, SAIP can also be applied to other methods that combine prior and likelihood, such as DiffGrad, and it consistently improves reconstruction quality across challenging settings, while preserving computational efficiency. The results suggest that adaptive scaling has potential for improving diffusion-based solvers.

5. REFERENCES

- [1] Antoni Buades, Bartomeu Coll, and Jean-Michel Morel, “A review of image denoising algorithms, with a new one,” *Multiscale Model. Simul.*, vol. 4, no. 2, pp. 490–530, 2005.
- [2] Bahjat Kawar, Michael Elad, Stefano Ermon, and Jiaming Song, “Denoising diffusion restoration models,” *Advances in neural information processing systems*, vol. 35, pp. 23593–23606, 2022.
- [3] Marcelo Bertalmio, Guillermo Sapiro, Vincent Caselles, and Coloma Ballester, “Image inpainting,” in *Proceedings of the 27th annual conference on Computer graphics and interactive techniques*, 2000, pp. 417–424.
- [4] Andrew M Stuart, “Inverse problems: a bayesian perspective,” *Acta numerica*, vol. 19, pp. 451–559, 2010.
- [5] Emmanuel J. Candès and Michael B. Wakin, “An introduction to compressive sampling,” *IEEE Signal Process. Mag.*, vol. 25, no. 2, pp. 21–30, 2008.
- [6] Maryam Fazel, Emmanuel Candès, Ben Recht, and Pablo Parrilo, “Compressed sensing and robust recovery of low rank matrices,” in *2008 42nd Asilomar Conference on Signals, Systems and Computers*. IEEE, 2008, pp. 1043–1047.
- [7] Dmitry Ulyanov, Andrea Vedaldi, and Victor Lempitsky, “Deep image prior,” in *Proceedings of the IEEE conference on computer vision and pattern recognition*, 2018, pp. 9446–9454.
- [8] Alexander Quinn Nichol and Prafulla Dhariwal, “Improved denoising diffusion probabilistic models,” in *International conference on machine learning*. PMLR, 2021, pp. 8162–8171.

- [9] Yang Song, Jascha Sohl-Dickstein, Diederik P. Kingma, Abhishek Kumar, Stefano Ermon, and Ben Poole, “Score-based generative modeling through stochastic differential equations,” *CoRR*, vol. abs/2011.13456, 2020.
- [10] Hyungjin Chung, Jeongsol Kim, Michael Thompson McCann, Marc Louis Klasky, and Jong Chul Ye, “Diffusion posterior sampling for general noisy inverse problems,” in *ICLR*. 2023, OpenReview.net.
- [11] Xiangming Meng and Yoshiyuki Kabashima, “Diffusion model based posterior sampling for noisy linear inverse problems,” in *Asian Conference on Machine Learning, 5-8 December 2024, Hanoi, Vietnam*, Vu Nguyen and Hsuan-Tien Lin, Eds. 2024, vol. 260 of *Proceedings of Machine Learning Research*, pp. 623–638, PMLR.
- [12] Jiaming Song, Arash Vahdat, Morteza Mardani, and Jan Kautz, “Pseudoinverse-guided diffusion models for inverse problems,” in *International Conference on Learning Representations*, 2023.
- [13] Badr Moufad, Yazid Janati, Lisa Bedin, Alain Durmus, Randal Douc, Eric Moulines, and Jimmy Olsson, “Variational diffusion posterior sampling with midpoint guidance,” *CoRR*, vol. abs/2410.09945, 2024.
- [14] Tongda Xu, Xiyan Cai, Xinjie Zhang, Xingtong Ge, Dailan He, Limin Sun, Jingjing Liu, Ya-Qin Zhang, Jian Li, and Yan Wang, “Rethinking diffusion posterior sampling: From conditional score estimator to maximizing a posterior,” *CoRR*, vol. abs/2501.18913, 2025.
- [15] Haoxuan Chen, Yinuo Ren, Martin Renqiang Min, Lexing Ying, and Zachary Izzo, “Solving inverse problems via diffusion-based priors: An approximation-free ensemble sampling approach,” *arXiv preprint arXiv:2506.03979*, 2025.
- [16] Masatoshi Uehara, Yulai Zhao, Chenyu Wang, Xiner Li, Aviv Regev, Sergey Levine, and Tommaso Biancalani, “Inference-time alignment in diffusion models with reward-guided generation: Tutorial and review,” *arXiv preprint arXiv:2501.09685*, 2025.
- [17] Yazid Janati, Badr Moufad, Mehdi Abou El Qassime, Alain Oliviero Durmus, Eric Moulines, and Jimmy Olsson, “A mixture-based framework for guiding diffusion models,” in *Forty-second International Conference on Machine Learning*, 2025.
- [18] Weichen Fan, Amber Yijia Zheng, Raymond A. Yeh, and Ziwei Liu, “Cfg-zero*: Improved classifier-free guidance for flow matching models,” *CoRR*, vol. abs/2503.18886, 2025.
- [19] Rayhan Zirvi, Bahareh Tolooshams, and Anima Anandkumar, “Diffusion state-guided projected gradient for inverse problems,” *arXiv preprint arXiv:2410.03463*, 2024.
- [20] Jonathan Ho and Tim Salimans, “Classifier-free diffusion guidance,” *CoRR*, vol. abs/2207.12598, 2022.
- [21] Bowen Song, Soo Min Kwon, Zecheng Zhang, Xinyu Hu, Qing Qu, and Liyue Shen, “Solving inverse problems with latent diffusion models via hard data consistency,” *ArXiv*, vol. abs/2307.08123, 2023.
- [22] Tero Karras, Samuli Laine, and Timo Aila, “A style-based generator architecture for generative adversarial networks,” in *IEEE Conference on Computer Vision and Pattern Recognition, CVPR*, 2019.
- [23] Fisher Yu, Yinda Zhang, Shuran Song, Ari Seff, and Jianxiong Xiao, “LSUN: construction of a large-scale image dataset using deep learning with humans in the loop,” *CoRR*, vol. abs/1506.03365, 2015.
- [24] Jooyoung Choi, Sungwon Kim, Yonghyun Jeong, Youngjune Gwon, and Sungroh Yoon, “Ilvr: Conditioning method for denoising diffusion probabilistic models,” *arXiv preprint arXiv:2108.02938*, 2021.
- [25] Alain Hore and Djemel Ziou, “Image quality metrics: Psnr vs. ssim,” in *2010 20th international conference on pattern recognition*. IEEE, 2010, pp. 2366–2369.
- [26] Zhou Wang, Alan C. Bovik, Hamid R. Sheikh, and Eero P. Simoncelli, “Image quality assessment: from error visibility to structural similarity,” *IEEE Trans. Image Process.*, vol. 13, no. 4, pp. 600–612, 2004.
- [27] Richard Zhang, Phillip Isola, Alexei A. Efros, Eli Shechtman, and Oliver Wang, “The unreasonable effectiveness of deep features as a perceptual metric,” in *2018 IEEE Conference on Computer Vision and Pattern Recognition, CVPR 2018, Salt Lake City, UT, USA, June 18-22, 2018*. 2018, pp. 586–595, Computer Vision Foundation / IEEE Computer Society.
- [28] Jonathan Ho, Ajay Jain, and Pieter Abbeel, “Denoising diffusion probabilistic models,” *CoRR*, vol. abs/2006.11239, 2020.